Investigation on the Influence of Amorphous-to-Crystalline Transformation on the Negative Thermo-Optic Properties of TiO_2 films

Honghwi Park[a], Jaedong Jung[a], Sunghwan Lee[c], and Hongsik Park[a,b]

[a] School of Electronic and Electrical Engineering, Kyungpook National University, Daegu 41566, Republic of Korea
[b] School of Electronics Engineering, Kyungpook National University, Daegu 41566, Republic of Korea
[c] School of Engineering Technology, Purdue University, West Lafayette, Indiana 47907, USA

In this work, we systematically investigate the structure-property relationship of atomic-layer-deposited TiO_2 to identify governing factors that determines the negative thermo-optic property of TiO_2, and we demonstrate negatively-enhanced thermo-optic coefficient (TOC) values (-1.8 to -2.3×10^{-4} /°C) from the visible to the near-infrared regime via mild-thermal budget processing. Structural characterizations based on X-ray diffraction and reflectivity, and temperature-dependent refractive index measurements based on spectroscopic ellipsometry prove that higher crystallinity of anatase TiO_2 leads to greater negative TOC values, ascribed to the higher film density and lower porosity compared to amorphous states. In addition, through the Prod'homme model and bandgap analysis, we also report that the negative TOC of TiO_2 is more influenced by the volume expansion than the polarizability.

Introduction

Temperature dependence of the refractive index is of particular importance for advanced photonic devices because their optical properties and phenomena are related to the refractive index. This dependence is defined by the thermo-optic coefficient (TOC), dn/dT, where n and T are the refractive index of a material and temperature, respectively. The refractive indices of conventional semiconductors (Si, Ge, and GaAs), which are widely used in fabrication of photonic devices, are known to increase with increasing temperature (i.e., positive TOC) and the TOC values of these materials are as high as over 1×10^{-4} /°C (1,2). Such large positive TOCs lead to significant instability of the optical performance of the photonic devices in response to temperature variations (3). To overcome the performance instability due to positive TOCs, athermal photonic device schemes that utilize materials with negative TOCs have been suggested, in which the temperature-related performance instability is mitigated by compensating the thermally-induced changes in refractive index (4-16).

One straightforward method to realize athermal devices is to overlay a cladding with large negative TOCs on photonic devices fabricated with positive-TOC materials. Since most polymers are known to have negative TOCs, polymer-based materials with large

negative TOCs such as urethane acrylate polymer (-4.2×10^{-4}/°C) and polysiloxane-based liquid polymer (-2.4×10^{-4}/°C) have been typically used in fabrication of athermal photonic devices (7,8). However, the use of polymers can be limited by their relatively poor complementary metal–oxide–semiconductor (CMOS) compatibility (i.e., heat/humidity sensitivity, weak mechanical strength, and dissimilar surface conditions with Si). Therefore, development and/or finding of inorganic-based oxides with large negative TOCs is of crucial for athermal applications in modern photonic integrated circuits (ICs), considering their excellent compatibility with the current standard Si CMOS technology.

Titanium dioxide (TiO_2) has long been hailed in various optoelectronic applications, including metaphotonics and photovoltaics, on account of its high refractive index, low loss tangent, and excellent transparency at a broad range of wavelengths. Moreover, TiO_2 has been known to have quite negative TOCs ranging from -5×10^{-5} /□ to -2.1×10^{-4} /□ (16,17); hence, it can enable athermalization of photonic devices. Furthermore, high-quality TiO_2 films can be deposited by well-established vacuum processes such as sputtering, chemical vapor deposition (CVD), and atomic layer deposition (ALD), which enables sophisticated and advanced optoelectronic applications. Thus, TiO_2 has been considered a promising inorganic material for athermal applications and the several previous studies have reported TiO_2-based athermalization schemes for temperature-insensitive advanced photonic devices (9–16). However, such technology to be more viable, it is important to establish strategies to engineer and obtain an enhanced negative TOC of TiO_2 with fundamental understanding of processing-structure-property relationships. The present study includes systematical investigations on the structure-property relationship of atomic-layer-deposited TiO_2 to identify governing factors that determines the negative thermo-optic property of TiO_2. The thermo-optic properties of TiO_2 are evaluated by refractive index measurements at various temperatures and wavelengths. The results are then correlated with the amorphous/crystalline structures.

Experimental

Deposition of TiO_2 Films

60-nm-thick TiO_2 films were deposited on single-crystalline Si (100) substrates through a thermal ALD system at 170 °C. In the deposition process, tetrakis-dimethylamino titanium (TDMAT) and water (H_2O) were used as the precursor and oxidant, respectively. Each deposition cycle in the ALD process was composed of 0.2-s TDMAT exposure, 10-s N_2 purge, 0.2-s H_2O exposure, and 10-s N_2 purge. The deposition rate was ~0.4 Å/cycle. The as-deposited TiO_2 films were subsequently annealed at 600 °C for 2 min by a rapid thermal annealing (RTA) process at an O_2 atmosphere with a flow rate of 2 slm.

Characterization Details

The refractive index of the TiO_2 films was measured with a spectroscopic ellipsometry (SE) system (Auto SE, HORIBA Jobin Yvon Inc.) in wavelengths of 440–1600 nm at an incident angle of 70°. In the measurement, the refractive index of the TiO_2 films was determined by the Forouhi-Bloomer dispersion model. The crystalline structure

and density/porosity of the TiO_2 films were evaluated by X-ray diffraction (XRD) and reflectivity (XRR) measurements (Empyrean diffractometer, Malvern Panalytical Inc.) with Cu *Kα* radiation operated at 40 kV and 25 mA. The surface morphology and cross-sectional microstructure were evaluated by atomic force microscopy (AFM, Park Systems NX20) and scanning electron microscopy (SEM, Hitachi SU8220). The optical bandgap was measured with a UV-Vis spectrometer (Cary 50, Varian Inc.) in wavelengths of 250–1000 nm.

Results and Discussion

Thermally-Induced Crystal Phase Transformation

The XRD spectra of ALD-TiO_2 films before and after 2-min RTA at 600 °C are shown in Figure 1. In the case of the as-deposited TiO_2, noticeable crystalline features are not observed in the XRD spectrum (black line). On the contrary, the evolution of crystalline phases are clearly observed in the XRD spectrum of the annealed TiO_2 (red line). The XRD patterns from the annealed TiO_2 show strong crystalline diffractions at the characteristic peak of poly-crystalline anatase TiO_2 with (101), (004), (200), (105), (211), (204), (116), (220), and (215) orientations. This diffraction characteristics agree with the well-known reference of anatase TiO_2 (JCPDS 21-1272). Meanwhile, no rutile phase of TiO_2 is observed in the XRD patterns owing to the insufficient annealing temperature. Typically, the rutile phases of TiO_2 are transformed by annealing at temperatures over ~800–900 °C, while anatase phases are transformed at temperatures from ~300–400 °C.

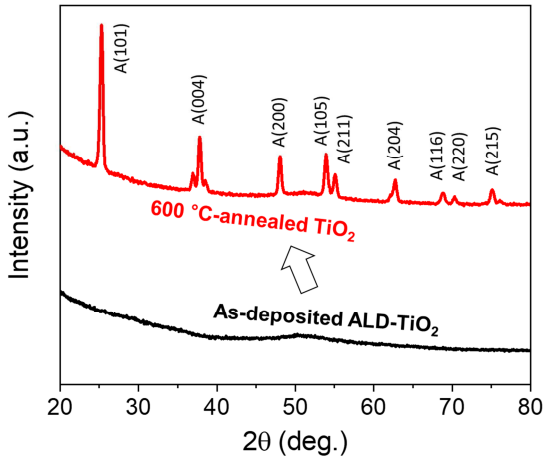

Figure 1. XRD spectra of the ALD-TiO_2 films of as-deposited (black) and 600 °C-annealed (red), where the amorphous-to-crystalline transformation is observed after RTA.

The AFM topographic images of the TiO_2 films before and after 2-min RTA at 600 °C are shown in Figure 2(a). The change in surface morphology is noticeably observed due to the annealing process (i.e., grain-like features have emerged). Root-mean-squared (RMS) surface roughness of the as-deposited TiO_2 is 4.4 Å, which increases to 6 Å after annealing. This is attributed to the enhanced poly-crystalline states with grains. In addition to the AFM images, such change in microstructures is also observed in the cross-sectional SEM images, as shown in Figure 2(b). The formation of

grains is observed after RTA. The film thickness is approximately 60 nm for both the as-deposited and 600 °C-annealed TiO_2 samples. The results in Figure 1 and 2 clearly show that the short-time RTA process leads to the amorphous-to-crystalline transformation (i.e., formation of the anatase TiO_2).

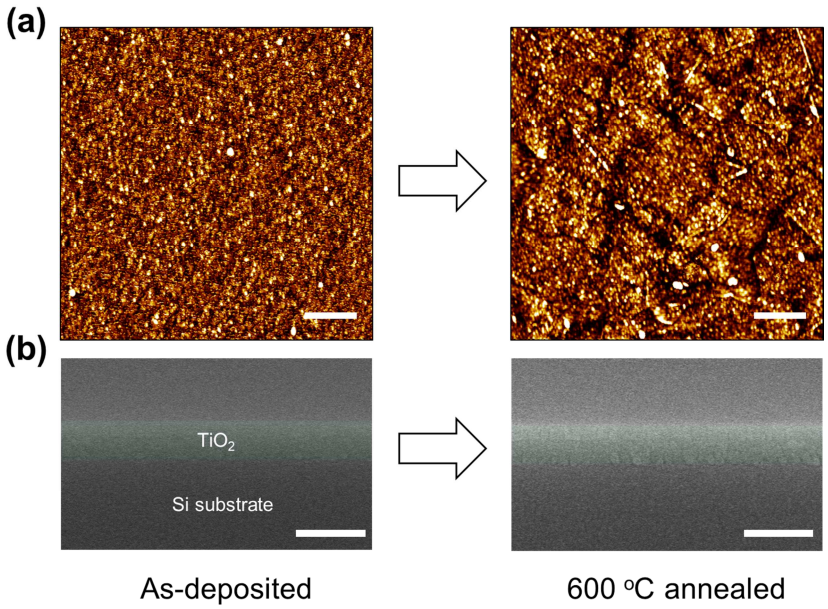

Figure 2. (a) AFM topographic and (b) cross-sectional SEM images of ALD-TiO_2 films of as-deposited (left) and 600 °C-annealed (right), where the formation of grains is clearly observed after RTA. The color and brightness of the TiO_2 films in the SEM images have been adjusted to make them more visible. The scale bars in the AFM and SEM images are 300 and 100 nm, respectively.

Enhancement of Refractive Index

Figure 3(a) shows the average refractive index of the ALD-TiO_2 films before and after RTA, which is determined with a SE measurement system at a wavelength of 632.8 nm under ambient conditions. The refractive index of the as-deposited film is 2.44, which increases to 2.54 after 600 °C annealing. The enhanced refractive index value is comparable to that for bulk anatase TiO_2 of ~2.57 (18). This enhancement after annealing is related to the crystalline phase transformation of TiO_2 in that the enhanced crystalline state induces an increase in packing density and a decrease in porosity. Thus, we first performed the XRR measurements to investigate the film density and porosity, and the measured XRR spectra of the TiO_2 films near the critical angle for reflection are shown in Figure 3(b). The determined critical angles for the TiO_2 films are shown by the dashed arrows: 0.266° for as-deposited TiO_2 and 0.272° for 600 °C-annealed TiO_2. Then, the film density (ρ) was calculated as follow (18):

$$\rho = (\pi A \theta_c)/(r_e \lambda^2 Z N_A) \quad [1]$$

where A is the mass number, θ_c is the critical angle, r_e is the classical electron radius, λ is the X-ray wavelength, Z is the atomic number, and N_A is the Avogadro's number. The determined film density of the TiO_2 films is shown in Figure 3(c). The film density increases from 3.53 g/cm^3 for as-deposited TiO_2 to 3.7 g/cm^3 after RTA at 600 °C. Note

that the film density of the annealed TiO_2 reaches to that of bulk anatase one (3.78 g/cm^3). Based on the estimated film density, we also investigated porosity of both the TiO_2 films (as-deposited and annealed) to identify the effect of that on the refractive index. The porosity was calculated from (19):

$$P = (1 - d_p/d) \times 100\ (\%) \qquad [2]$$

where d_p is the density of porous films and d is that of pure anatase TiO_2. As shown in Figure 3(d), the porosity is reduced from 6.6% for the as-deposited TiO_2 film to 2.1% after RTA at 600 °C. These results indicate that the thermally-induced enhanced crystallinity leads to the improving the film quality (i.e., increased density and reduced porosity), which ultimately leads to the increasing the refractive index.

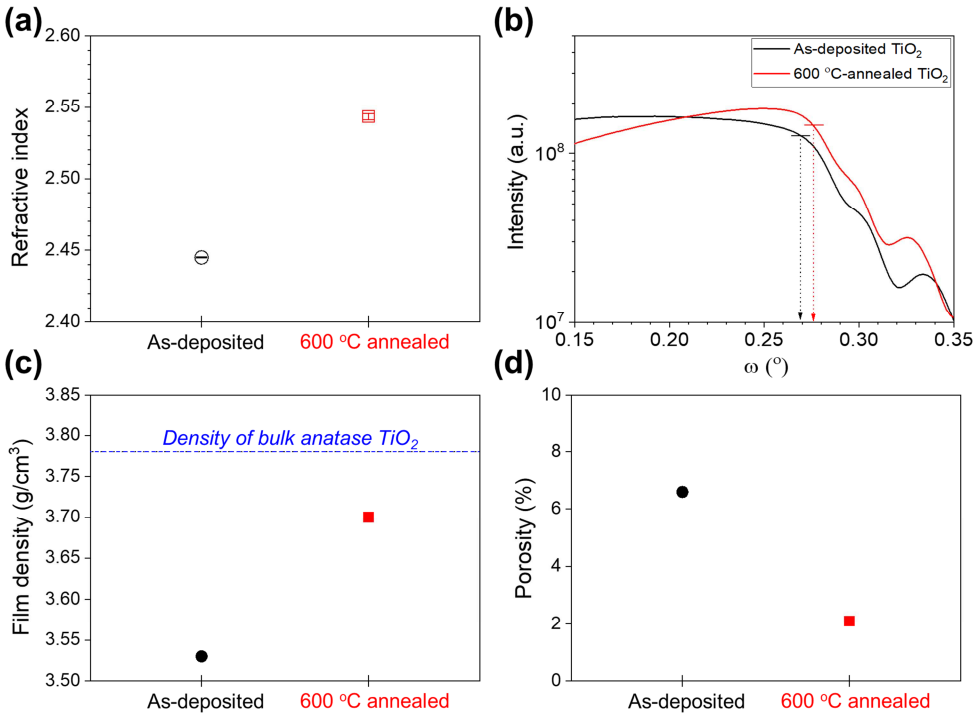

Figure 3. (a) Average refractive index of as-deposited and 600 °C-annealed TiO_2 films measured at a SE wavelength of 632.8 nm under ambient conditions. (Error bars are less than the marker size). (b) XRR spectra of the TiO_2 films near the critical angle for reflection. The dashed arrows indicate the critical angles of the TiO_2 films. (c) Film density of as-deposited and 600 °C-annealed TiO_2 determined from their XRR spectrum. The dashed blue line indicates the density of bulk anatase TiO_2 (3.78 g/cm^3). (d) Porosity of the TiO_2 films estimated from their film density.

Enhancement of Negative Thermo-Optic Properties

Figure 4 shows the temperature dependence of the average refractive index of the ALD-TiO_2 films before and after RTA at various wavelengths, in which the refractive index decreases along with the temperature (30–70°) at all the samples and wavelengths. To investigate the thermo-optic properties of the TiO_2 films, we extracted the TOCs (i.e., dn/dT) by linear regression analysis. As a result, all the TOCs of the TiO_2 samples are negative at all the wavelengths, and TOC further decreases (i.e., negatively enhances)

after RTA at 600 °C. At a wavelength of (a) 632.8 nm, (b) 1000 nm, and (c) 1550 nm, the TOC of TiO_2 decreases from -1.13×10^{-4} /°C (as-deposited) to -1.79×10^{-4} /°C (annealed), from -1.4×10^{-4} /°C (as-deposited) to -2.15×10^{-4} /°C (annealed), and from -1.55×10^{-4} /°C (as-deposited) to -2.3×10^{-4} /°C (annealed), respectively. In other words, the negative TOC of TiO_2 is enhanced by ~1.5 times at all the wavelengths after the amorphous-to-crystalline phase transformation.

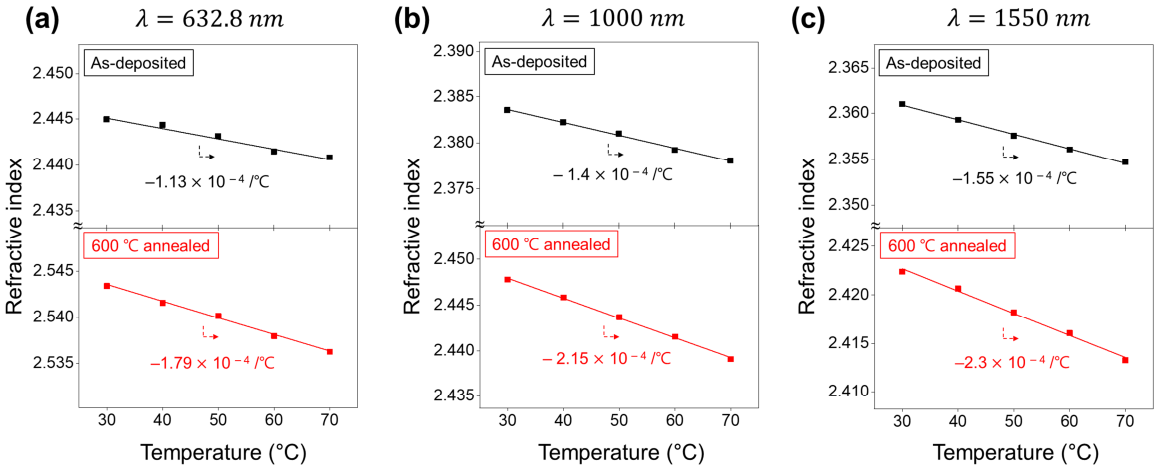

Figure 4. Temperature dependence of the average refractive index of the TiO_2 films of as-deposited (black) and 600 °C-annealed (red) at a SE wavelength of (a) 632.8 nm, (b) 1000 nm, and (c) 1550 nm. The slopes of the plots indicate the TOCs (i.e., *dn/dT*), which were extracted by linear regression analysis.

The enhanced negative TOC after annealing can be explained with the increased crystallinity and the Prod'homme model which is widely used to account for the temperature-dependent refractive index (20). According to the Prod'homme model, the *dn/dT* (i.e., TOC) is determined by two-competing factors (thermal expansion coefficient and electronic polarizability) as follow:

$$dn/dT \propto (\Phi - \beta) \quad [3]$$

where $\Phi = (1/P)(dP/dT)$ is the temperature coefficient of the electronic polarizability and $\beta = (1/V)(dV/dT)$ is the volume expansion coefficient. The Prod'homme model shows that TOC is negative when the influence of the volume expansion is larger than that of the polarizability (i.e., $\beta > \Phi$). This means that the negative TOC of TiO_2 is originated from the volume expansion coefficient larger than the temperature coefficient of the electronic polarizability, and the enhanced negative TOC after RTA is from the increased volume expansion coefficient caused by the increased crystallinity. To reveal this more clearly, we performed the UV-Vis measurements and extracted the optical bandgap of TiO_2 films from Tauc plots ($\alpha h\nu^{1/2}$ *vs.* $h\nu$) as shown in Figure 5(a). There is no noticeable narrowing and/or broadening in optical bandgap of TiO_2 before and after annealing, all of which were estimated to ~3.25 eV at both TiO_2 samples (as-deposited and annealed). This indicates that the change in temperature coefficient of the electronic polarizability is expected to be very small. On the other hand, the volume expansion of TiO_2 in response to temperature variations has been reported to be high (21). Figure 5(b) show the calculated volume expansion coefficient as a function of the temperature for bulk anatase TiO_2 through Rietveld analysis, where the volume expansion coefficient increases with

increasing temperature. Thus, we could conclude that the volume expansion coefficient, rather than the electronic polarizability coefficient, is the dominant factor determining the negative TOC of TiO_2. Furthermore, the enhancement of the negative TOC after annealing is attributed to the amorphous-to-crystalline phase transformation. The reason is that randomly disordered nature of the amorphous phase may limit temperature-related volume changes compared to the ordered crystalline anatase phase, and the highly anisotropic lattice structure of anatase TiO_2 may facilitate a higher temperature-related volume changes than the amorphous phase (21).

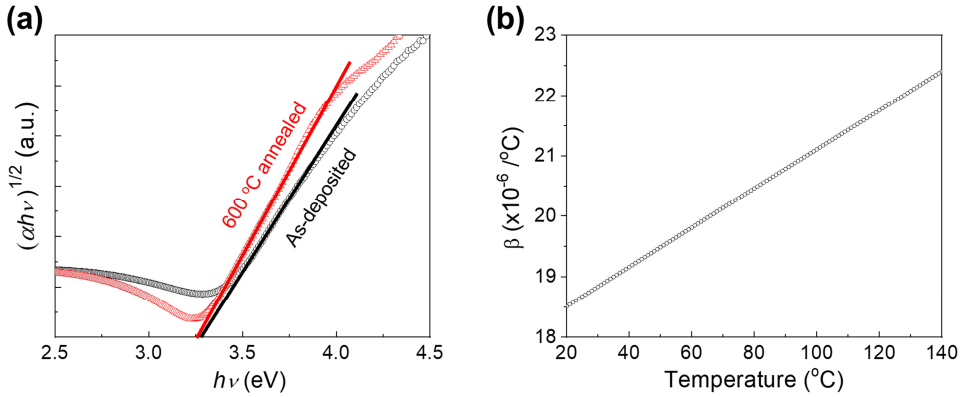

Figure 5. (a) Tauc plots ($\alpha h\nu^{1/2}$ *vs.* $h\nu$) for the extraction of optical bandgap of TiO_2. (b) Volume expansion coefficient (β) of anatase TiO_2 as a function of the temperature, where the β increases along with the temperature.

Conclusions

In summary, we investigated the structure-property relationship of atomic-layer-deposited TiO_2 to identify governing factors that determines the negative thermo-optic property of TiO_2. Mild-thermal budget processing (600 °C RTA, 2 min) enabled the amorphous-to-crystalline transformation of TiO_2 with an increased film density and porosity, through which the negatively-enhanced TOC at wavelengths from the visible to the near-infrared regime was achieved (from -1.8 to -2.3×10^{-4} /°C). In order to reveal the origin of enhancement of the refractive index and negative TOC, various characterizations based on XRD, XRR, AFM, SEM, UV-Vis, and SE measurements were performed, and the results were correlated with the crystalline structure, film quality, and optoelectronic properties.

Acknowledgments

This work was supported in part by the National Research Foundation of Korea (NRF) grant funded by the Korea government (MSIT) (2020R1A4A1019518), the NRF grant funded by the Korea government (MSIT) (2019R1A2C1088324), and the Bio & Medical Technology Development Program of the NRF funded by the Ministry of Science & ICT (2017M3A9G8083382). SL thanks the supports from the U.S. National Science Foundation (NSF, Award No. ECCS-1931088), the Purdue Research Foundation (Award No. 60000029) and the Polytechnic RDE SEED program.

References

1. B. Frey, D. Leviton, and T. Madison, in *Proc. SPIE*, **6273**, 62732J (2006).
2. F. Della Corte, G. Cocorullo, M. Iodice, and I. Rendina, *Appl. Phys. Lett.*, **77**, 1614–1616 (2000).
3. G. Reed, G. Mashanovich, F. Gardes, and D. Thomson, *Nat. Photonics*, **4**, 518–526 (2010).
4. F. Qiu, A. Spring, F. Yu, I. Aoki, A. Otomo, and S. Yokoyama, *Appl. Phys. Lett.*, **102**, 1–4 (2013).
5. J. Bovington, R. Wu, K. –T. Cheng, and J. Bowers, *Opt. Express.*, **22**, 661–666 (2014).
6. J. Bovington, S. Srinivasan, and J. Bowers, *Opt. Express.*, **22**, 19357–19364 (2014).
7. J. Teng, P. Dumon, W. Bogaerts, H. Zhang, X. Jian, X. Han, M. Zhao, G. Morthier, and R. Baets, *Opt. Express.*, **17**, 14627–14633 (2009).
8. P. Alipour, E. Hosseini, A. Eftekhar, B. Momeni, and A. Adibi, in *Conference on Lasers and Electro-Optics*, CMAA4, pp 1–2 (2009).
9. O. Reshef, K. Shtyrkova, M. Moebius, S. Griesse–Nascimento, S. Spector, C. Evans, E. Ippen, and E. Mazur, *J. Opt. Soc. Am. B.*, **32**, 2288–2293 (2015).
10. S. Feng, K. Shang, J. Bovington, R. Wu, B. Guan, K. –T. Cheng, J. Bowers, and S. Yoo, *Opt. Express.*, **23**, 25653–25660 (2015).
11. S. Feng, K. Shang, J. Bovington, R. Wu, K. Cheng, J. Bowers, and S. Yoo, in *IEEE Photonics Conf.*, pp 116–117 (2014).
12. B. Guha, J. Cardenas, and M. Lipson, *Opt. Express.*, **21**, 26557–26563 (2013).
13. H. Hirota, M. Itoh, M. Oguma, and Y. Hibino, *IEEE Photonics Technol. Lett.*, **17**, 375–377 (2005).
14. T. Lipka, L. Moldenhauer, J. Müller, and H. Trieu, *Opt. Express.* **23**, 20075–20088 (2015).
15. S. Zhu, G. Lo, and D. Kwong, *Opt. Express.*, **21**, 12699–12712 (2013).
16. S. Djordjevic, K. Shang, B. Guan, S. Cheung, L. Liao, J. Basak, H. –F. Liu, and S. Yoo, *Opt. Express.*, **21**, 13958–13968 (2013).
17. H. Xie, F. Ng, and X. Zeng, *Thin Solid Films*, **517**, 5066–5069 (2009).
18. P. Bergese, E. Bontempi, and L. Depero, *Appl. Surf. Sci.* **253**, 28–32 (2006).
19. G. Vicente, A. Morales, and M. Gutierrez, *Thin Solid Films*, **391**, 133–137 (2001).
20. L. Prod'Homme, *Phys. Chem. Glasses*, **1**, 119–122 (1960).
21. D. Hummer, P. Heaney, and J. Post, *Powder Diffr.*, **22**, 352–357 (2007).